ELECTROPLATING

Electroplating lithium transition metal oxides

Huigang Zhang,[1]* Hailong Ning,[2]* John Busbee,[2] Zihan Shen,[1] Chadd Kiggins,[2] Yuyan Hua,[2] Janna Eaves,[2] Jerome Davis III,[2] Tan Shi,[2] Yu-Tsun Shao,[3] Jian-Min Zuo,[3,4] Xuhao Hong,[1] Yanbin Chan,[1] Shuangbao Wang,[1] Peng Wang,[1] Pengcheng Sun,[3] Sheng Xu,[5] Jinyun Liu,[3] Paul V. Braun[2,3,4,6,7]*

Materials synthesis often provides opportunities for innovation. We demonstrate a general low-temperature (260°C) molten salt electrodeposition approach to directly electroplate the important lithium-ion (Li-ion) battery cathode materials $LiCoO_2$, $LiMn_2O_4$, and Al-doped $LiCoO_2$. The crystallinities and electrochemical capacities of the electroplated oxides are comparable to those of the powders synthesized at much higher temperatures (700° to 1000°C). This new growth method significantly broadens the scope of battery form factors and functionalities, enabling a variety of highly desirable battery properties, including high energy, high power, and unprecedented electrode flexibility.

INTRODUCTION

Lithium transition metal oxides (LTMOs), which are typically synthesized in powder form via solid-state reactions at 700° to 1000°C, are nearly universally applied as cathode materials in Li-ion batteries. Because the current collector substrates used for Li-ion battery electrodes degrade at the LTMO synthesis temperatures (*1*), cathodes are made by slurry-casting the presynthesized LTMO powder onto either metal foils for conventional batteries or porous scaffolds (for example, fiber mats and open-cell foams) for emerging three-dimensional (3D) (*2*–*4*) and flexible battery designs (*5*, *6*). However, the electrochemical and mechanical properties of slurry-cast electrodes are often limited by weak interconnections between particles and between the particles and the substrate (*7*, *8*). We suggest that conformal electrodeposition of high-quality LTMOs would provide opportunities to enhance battery performance (energy density, power density, and flexibility) and broaden the scope of available electrode form factors (size, shape, porosity, and 3D integration). Whereas LTMOs are primarily used in batteries, LTMOs have also been considered for use as oxygen reduction catalysts (*9*) and anticorrosion layers (*10*), two applications where conformal deposition is important. Although atomic layer deposition (ALD) has been demonstrated to conformally grow LTMO films, as reviewed by Liu and Sun (*11*), the crystallinity and electrochemical performance of ALD-grown LTMOs is far inferior to those of conventionally synthesized LTMO powders. ALD is also not appropriate for thick films because of the very slow deposition rate. Before this report, electrodeposition, although successful for the syntheses of some oxide ceramics (*12*, *13*), had not been demonstrated for the growth of high-quality LTMOs (*14*–*20*). Previously electroplated LTMOs exhibited poor electrochemical performance because of the inclusion of water, undesired cations, transition metals at incorrect valance states, and disorder in the crystal structure (*21*, *22*).

Here, we report a general low-temperature (~260°C) molten salt electrodeposition methodology to directly grow LTMOs (including layered $LiCoO_2$, spinel $LiMn_2O_4$, and Al-doped $LiCoO_2$), with crystallinities, and electrochemical performances, comparable to those made by traditional high-temperature (700° to 1000°C) routes. This method is compatible with a variety of conventional (for example, Al foil) and mesostructured current collectors, providing opportunities to realize new electrode architectures and functionalities. We demonstrate that a ~25-μm-thick, ~80% dense $LiCoO_2$ film can be directly electroplated on an Al foil, and the resultant full cell can deliver high-rate discharge up to at least 20 C. The high solubility of the transition metal salts in the molten hydroxide plating solution (see section SI), in conjunction with the plating solution's high ionic conductivity, minimizes the depletion of precursor ions during electrodeposition, allowing the formation of highly uniform deposits through mesostructured foams (see section SII) for ultrahigh areal capacities (for example, ~20 mA·hour cm^{-2} for the 0.5-mm-thick $LiCoO_2$ electrode). When LTMOs are electroplated on a flexible network, such as a carbon nanofiber (CNF) paper (see figs. S1 and S2 and section SIII), intimate contact between the plated material and the current collector endows the electrode with superior flexibility, enabling fabrication of an ultraflexible battery using this cathode and a CNF-based anode that can cycle after being repeatedly bent 10,000 times from 0° to 180°.

RESULTS AND DISCUSSION

Electrodeposition of $LiCoO_2$ is carried out at 260°C in a near-eutectic mixture of LiOH, KOH, and CoO. To investigate the $LiCoO_2$ formation, cyclic voltammograms (CVs) of various working electrodes (CNF, Pt, Co, and Ni) are recorded using a Co wire as the quasi-reference electrode (see section SIV). In a CoO-free molten LiOH-KOH bath, gases are evolved at the CNF (Fig. 1A) and the Pt (Fig. 1B) working electrodes when the potential is greater than 1.2 V (slope S1) or below −0.25 V (slope S2), as the result of the oxidation ($2OH^- \rightarrow H_2O + 1/2O_2 + 2e$) and reduction ($2H_2O \rightarrow 2OH^- + H_2 - 2e$) of the hydroxide melt, respectively. Once CoO is added to the hydroxide melt (Fig. 1A), a hump at 1.0 V (P2) appears in the oxidation scan, corresponding to the formation of $LiCoO_2$ via electrooxidation of Co^{2+}. In the reduction scan, Co^{2+} is reduced to Co metal below 0 V

[1]National Laboratory of Solid State Microstructures, College of Engineering and Applied Sciences, Collaborative Innovation Center of Advanced Microstructures, Institute of Materials Engineering, Nanjing University, Nanjing 210093, China. [2]Xerion Advanced Battery Corporation, 60 Hazelwood Drive, Champaign, IL 61820, USA. [3]Department of Materials Science and Engineering, University of Illinois at Urbana-Champaign, Urbana, IL 61801, USA. [4]Frederick Seitz Materials Research Laboratory, University of Illinois at Urbana-Champaign, Urbana, IL 61801, USA. [5]Department of NanoEngineering, University of California, San Diego, La Jolla, CA 92093, USA. [6]Beckman Institute for Advanced Science and Technology, University of Illinois at Urbana-Champaign, Urbana, IL 61801, USA. [7]Department of Chemistry, University of Illinois at Urbana-Champaign, Urbana, IL 61801, USA.
*Corresponding author. Email: hgzhang@nju.edu.cn (H.Z.); h.ning@xerionbattery.com (H.N.); pbraun@illinois.edu (P.V.B.)

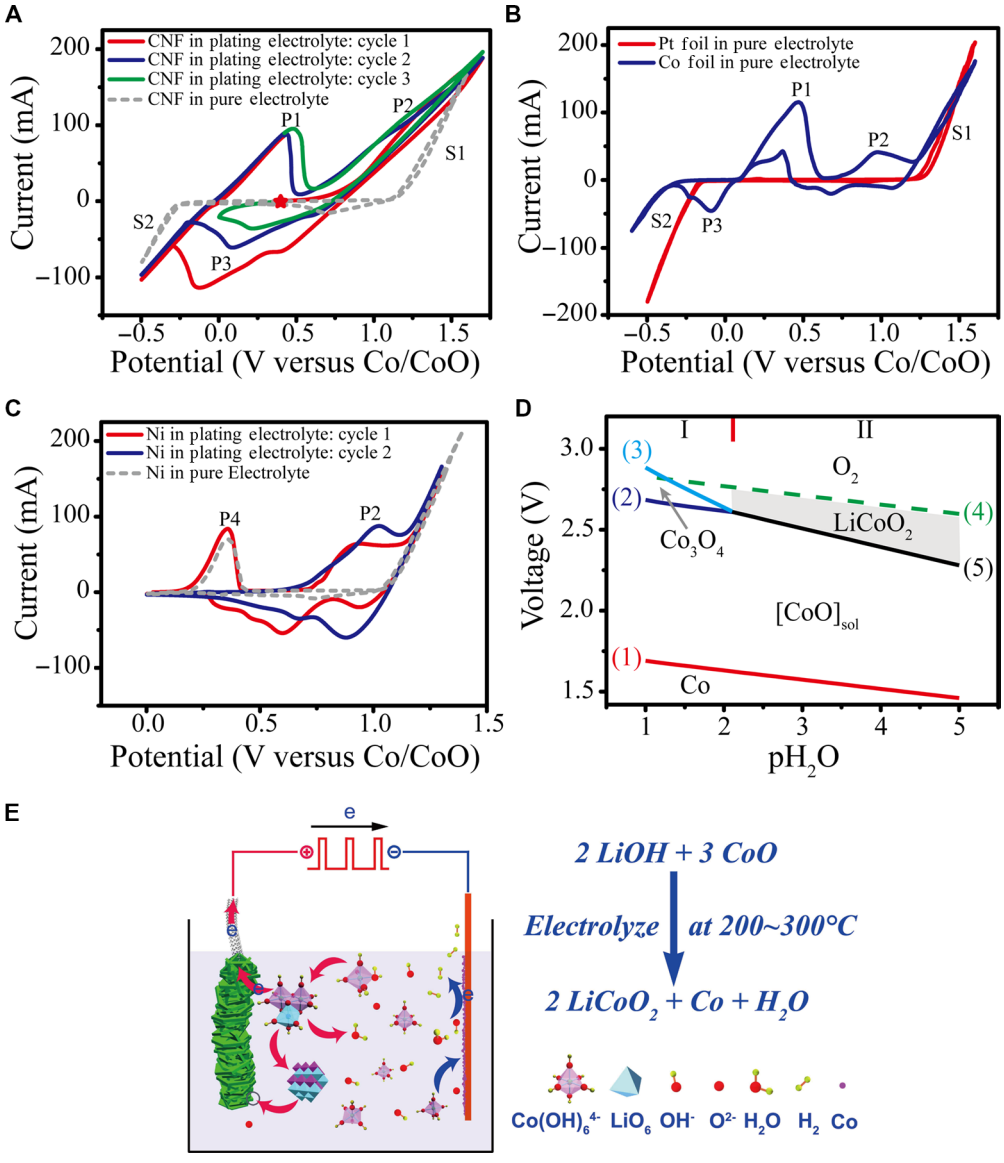

Fig. 1. Cyclic voltammetric and electrochemical modeling of KOH-LiOH-CoO eutectic systems. (**A**) CVs of CNF in pure and CoO-containing LiOH-KOH melts. (**B**) CVs of Co and Pt foils in pure LiOH-KOH melt. (**C**) CVs of Ni foil in pure and CoO-containing LiOH-KOH melts. (**D**) Potential-pH_2O diagram of the LiOH-KOH-CoO eutectic system. (**E**) Schematic illustration of electrodeposition process. All the CV measurements start from an oxidative scan.

(P3). When the working electrode is Co metal, Co is first oxidized to Co^{2+} around peak P1 (Fig. 1, A and B) and then transformed to $LiCoO_2$ at P2 (Fig. 1, A and B). Ni is oxidized at ~0.3 V (P4) in a pure hydroxide melt but exhibits no peak at 1.0 V (Fig. 1C). When CoO is added to the melt, $LiCoO_2$ starts to form on the Ni electrode at 1.0 V and appears to fully passivate the surface as peak P4 disappears after the first CV scan. On the basis of this analysis, we deduce that $LiCoO_2$ can be electrodeposited in a near-eutectic hydroxide melt at 260°C via the following reaction: $2LiOH + 3CoO \rightarrow 2LiCoO_2 + Co + H_2O$.

The $LiCoO_2$ formation mechanism is further evaluated by the thermodynamic potential-pH_2O diagram (Pourbaix diagram). In a hydroxide melt, H_2O acts as a Lux-Flood acid and accepts O^{2-}, turning into $2OH^-$. The acidity, pH_2O [defined as $-\log(\chi_{H_2O})$, where χ_{H_2O} is the concentration of H_2O in the melt], plays an important role in determining the electroplating potential of each material and the thermodynamic stability of each compound. Figure 1D depicts two electrochemical reaction regimes of greatest interest (see the modeling in section SV). Region I closely represents the conventional aqueous electrodeposition regime, in which Co_3O_4 is thermodynamically favorable because of the low formation potential (*23*, *24*). As the melt becomes more basic, Co_3O_4 becomes unstable, and at the proper potential, pure $LiCoO_2$ forms. In region II (the shaded area), the oxygen line is at a higher voltage than the $LiCoO_2$ formation line, suggesting that oxygen gas can spontaneously oxidize CoO to $LiCoO_2$, resulting in undesirable precipitation of $LiCoO_2$ in solution. $LiCoO_2$ electrodeposition is thus performed in an oxygen-free environment. The calculated phase diagram agrees well with the experimental CV result that it is possible to obtain $LiCoO_2$ in a hydroxide molten salt via an anodic electrochemical process, as shown in Fig. 1E.

Selective area electron diffraction is used to examine the electroplated $LiCoO_2$ and shows that the as-deposited material is O3-$LiCoO_2$ (O3 refers to the oxygen stacking in the crystal structure following ABCABC)

(see figs. S3 and S4 and section SVI for details). Nanobeam diffraction reveals extra weak reflections (Fig. 2A) along the edge of a hexagonal flake of the electroplated $LiCoO_2$, suggesting that the $R\bar{3}m$ symmetry is broken in this region. To further study the crystal microstructure of the electroplated $LiCoO_2$ and the impurity phases, we adopt the scanning electron nanobeam diffraction (SEND) technique to investigate a crystal flake with a 3-nm-diameter semi-convergent electron beam (see section SVII for details). The intensities of different reflections {hkl} are collected with respect to probe positions (fig. S5). As shown in Fig. 2A, the diffraction patterns obtained from the edge and

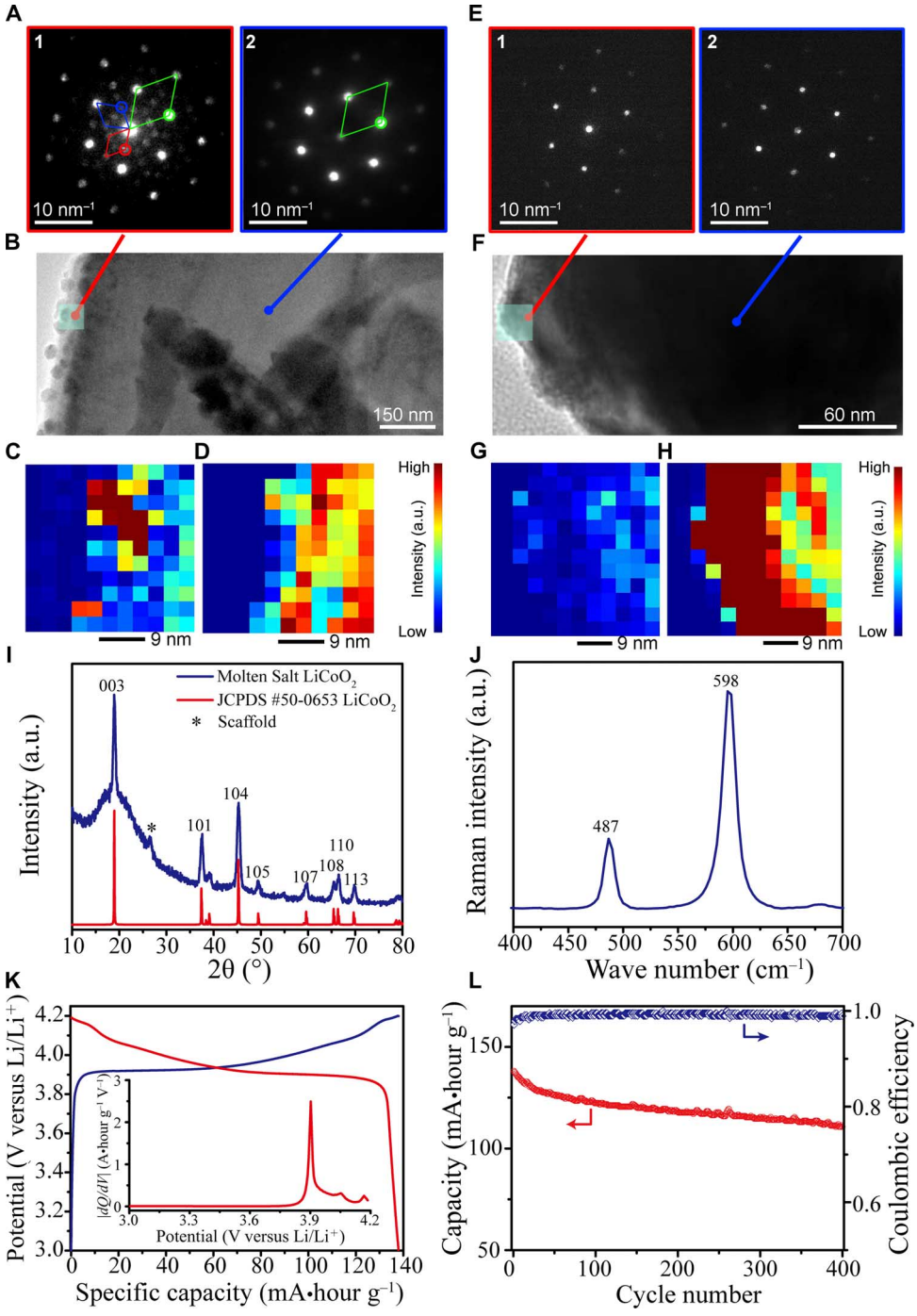

Fig. 2. Characterizations of electroplated $LiCoO_2$. (**A**) Diffraction patterns collected from the edge (1) and center (2) of an as-prepared $LiCoO_2$ flake and (**B**) its transmission electron microscopy (TEM) image. Diffraction mapping of (**C**) non-O3 (intensity multiplied by a factor of 20) and (**D**) O3 phases. a.u., arbitrary units. (**E**) Diffraction patterns of spots from the edge (1) and the center (2) of an annealed $LiCoO_2$ flake and (**F**) its TEM image. Diffraction patterns of (**G**) non-O3 (intensity multiplied by a factor of 20) and (**H**) O3 phases after annealing. XRD (**I**) and Raman spectroscopy (**J**) of the $LiCoO_2$ electrode. (**K**) Charge/discharge voltage profiles. Inset: $|dQ/dV|$ of the $LiCoO_2$ cathode (electroplated on an Al foil) versus a lithium electrode. (**L**) Cycling of the electrodeposited $LiCoO_2$ cathode versus a Li electrode at 1 C.

the center of the as-synthesized $LiCoO_2$ flake both show strong {110} diffractions belonging to the O3-$LiCoO_2$ phase (green parallelogram). The additional weak diffractions observed on the edge of the crystal are marked with blue and red circles. The intensities of non-O3 and O3 {110} diffractions across the green box in Fig. 2B are mapped with respect to the probe positions in Fig. 2 (C and D), respectively. It appears that there is an ~9-nm non-O3 layer present on the perimeter of a typical ~3-μm crystal flake, consisting of less than 0.06% of the as-deposited material. According to previous reports (*25*–*30*), these additional reflections may result from the stack shift, lithium staging/ordering, or a spinel-like intergrowth (fig. S4). The surface phase is most likely related to O2-$LiCoO_2$ (*31*, *32*). O3- and O2-$LiCoO_2$ share reflections at 7.08 nm^{-1}, but the O2 structure has extra diffraction spots at 4.12 nm^{-1} because of the ABAC oxygen stacking (*33*), which is in agreement with the electron diffraction (Fig. 2A). Previous reports have confirmed that O2-$LiCoO_2$ is thermally unstable and converts to the O3 phase upon annealing at ~400°C (*31*, *33*). After annealing at 400°C in Ar for 2 hours, the edge and center diffraction patterns are similar (Fig. 2, E and F), and the SEND mapping (Fig. 2, G and H) reveals that the diffraction intensity from the non-O3 impurity structure is significantly reduced (the intensity in Fig. 2G is multiplied 20-fold), indicating that the non-O3 impurity phase has been removed. A more detailed analysis of the possible structures and associated diffraction modeling is in section SVI.

X-ray diffraction (XRD) of the electrodeposited $LiCoO_2$ (Fig. 2I) agrees with layered $LiCoO_2$ (space group 166, $R\bar{3}m$). It is notable that the (108) and (110) peaks are split around ~66°, which has been widely accepted as the evidence of highly crystallized layered $LiCoO_2$ (*25*). Raman spectroscopy shows two well-defined peaks at 487 and 598 cm^{-1} (Fig. 2J), corresponding to the E_g and A_{1g} vibration modes of the layered rock-salt $LiCoO_2$ (*34*), which is usually only attainable via solid-state reaction at ~900°C (*34*–*36*). Figure 2K shows galvanostatic charge/discharge curves of the electroplated $LiCoO_2$ versus lithium. The well-defined plateaus (~3.9 V) and the sharp peaks in the *dQ/dV* curve further confirm that $LiCoO_2$ has an $R\bar{3}m$ structure with O3 stacking. This plated $LiCoO_2$ delivers a specific capacity of 138 mA·hour g^{-1} from 3 to 4.2 V and retains ~80% of the initial capacity after 400 cycles (Fig. 2L).

The conformal deposition of $LiCoO_2$ is demonstrated on a conventional Al metal foil current collector and two different carbon scaffolds (see sections SII and SIII for details), a mesoporous carbon foam (Fig. 3D) and a CNF network (Fig. 3G). Figure 3 (A and B) shows the scanning electron microscopy (SEM) images of planar $LiCoO_2$ films electroplated on both sides of the Al foil. Owing to the excellent

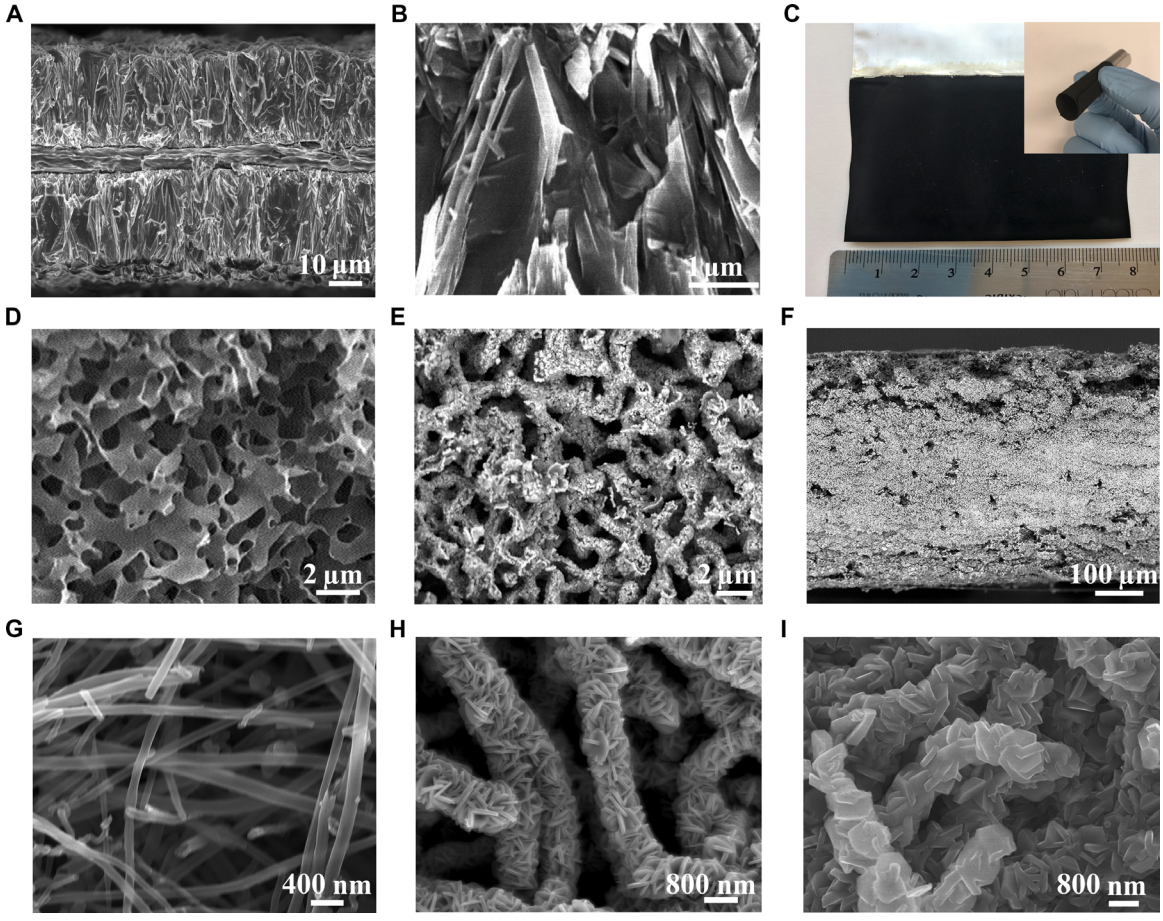

Fig. 3. Morphology of $LiCoO_2$ electroplated on various substrates. (**A**) SEM images of planar $LiCoO_2$ films (~20% porosity) electroplated on both sides of an Al foil. (**B**) Higher-magnification view of the $LiCoO_2$ coating. (**C**) Optical images of $LiCoO_2$ electroplated on the Al foil and this electrode rolled into a 5-mm-diameter tube (inset). SEM images of the open-cell carbon foam (**D**) and the $LiCoO_2$/carbon foam electrode (**E**). (**F**) Lower-magnification view of a ~0.5-mm-thick $LiCoO_2$/carbon foam electrode, with $LiCoO_2$ plated uniformly throughout the foam. SEM images of the 3D CNF scaffold (**G**) and the $LiCoO_2$ electrodes electroplated on this scaffold with ~1 mA·hour cm^{-2} loading (**H**) and ~3 mA·hour cm^{-2} loading (**I**).

electronic conductivity of $LiCoO_2$, it is possible to directly grow a nearly 200-μm-thick film (fig. S6). The porosity of the coating, which can be tuned from 10 to 60% by controlling the deposition voltage and duty cycle during the pulsed electroplating, provides the freedom to engineer the electrode flexibility. As demonstrated in Fig. 3C, an appropriate coating porosity (~20%), in conjunction with the strong coating adhesion to the Al foil, enables rolling a ~70-μm-thick electrode (Al foil thickness, 20 μm) at a 5-mm radius. In addition, the high solubility of CoO in the hydroxide melt and the high ionic conductivity of the plating solution minimizes ion depletion during electroplating, allowing uniform deposition of $LiCoO_2$ throughout thick (0.5 mm) carbon foam scaffolds with an areal loading of ~145 mg cm^{-2} (Fig. 3, E and F). Figure 3 (H and I) shows the SEM images of $LiCoO_2$/CNF electrodes, where the $LiCoO_2$ coating thickness is tuned by the electrodeposition time.

The intimate contact between the electroplated $LiCoO_2$ coating and the current collector minimizes the contact resistance, which has been shown to account for up to 25% of cell polarization in high-power cells (*37*). We suspect that it is a combination of excellent electrical contact between the $LiCoO_2$ and the current collector and the high intrinsic electrical conductivity of $LiCoO_2$ that allows these monolithic electrodes to exhibit excellent power. Figure 4 (A and B) shows the power and cycling performance of a pouch cell consisting of a $LiCoO_2$/Al foil cathode and a conventional graphite-based anode. The cell retains 75% of the 0.5-C capacity at a 10-C discharge, 55% of the 0.5-C capacity at a 20-C discharge, and ~80% of the initial capacity after 350 cycles, which are impressive results for a cell containing a $LiCoO_2$ cathode that contains no binders or conductive additives ($LiCoO_2$ layer is ~25 μm thick and ~80% dense).

When the active material is electroplated on 3D mesostructured current collectors, the power of the resultant electrodes is increased by the improved ion transports in the interconnected pores of the 3D electrode (*4*). As shown in Fig. 4D, a 100-μm-thick $LiCoO_2$/CNF electrode retains

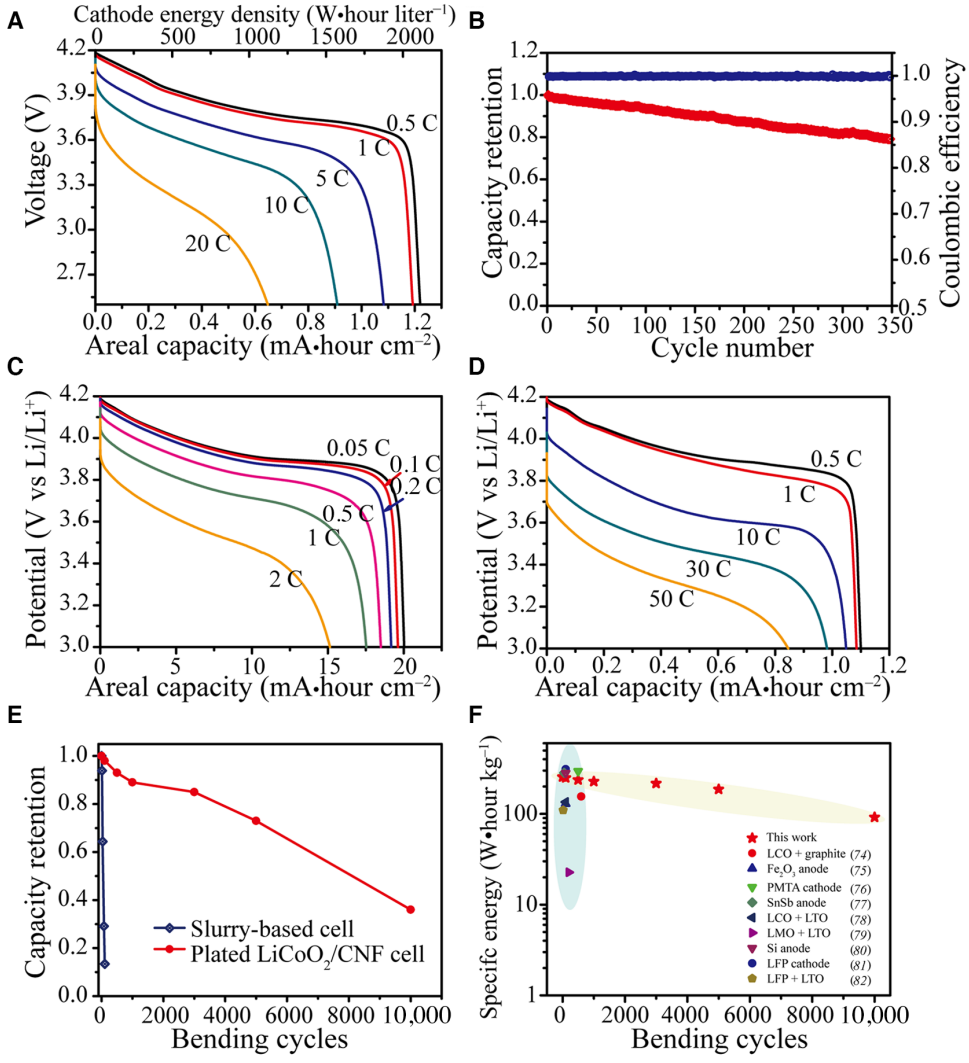

Fig. 4. Electrochemical and flexural properties of $LiCoO_2$ electrodes. Electrochemical performance of a full pouch cell consisting of a $LiCoO_2$/Al foil cathode and a conventional anode: (**A**) capacity retentions of the full cell at varied discharge rates and (**B**) cycling of the full cell at 1 C. (**C**) Capacity retentions of a ~20 mA·hour cm^{-2} $LiCoO_2$/carbon foam electrodes at varied discharge rates. (**D**) Capacity retentions of a ~1.1 mA·hour cm^{-2} $LiCoO_2$/CNF electrodes at varied discharge rates. (**E**) Capacity retention of the $LiCoO_2$/CNF-based and $LiCoO_2$ slurry–based full cells after cyclic bending of 180° to an ~5-mm radius. (**F**) Energy density and flexural performance of our and other flexible batteries. LCO, lithium cobalt oxide; PMTA, pyromellitic dianhydride-tris(2-aminoethyl)amine; LTO, lithium titanium oxide; LMO, lithium manganese oxide; LFP, lithium iron phosphate.

90% of the 0.5-C capacity (areal capacity: 1.1 mA·hour cm^{-2}) at a 30-C discharge and ~76% of the 0.5-C capacity at a 50-C discharge. An ~0.5-mm-thick $LiCoO_2$/carbon foam electrode delivers ~20 mA·hour cm^{-2} at C/5 to C/20 and ~15 mA·hour cm^{-2} at 2 C (Fig. 4C), a much better rate capacity relative to other thick electrodes with significantly smaller loadings (*38*, *39*).

Bulk $LiCoO_2$ is brittle, but, when adhered to the flexible CNF core, it provides a very flexible cathode. We assemble a full cell using a $LiCoO_2$/CNF cathode and a graphitized CNF anode. The voltage profiles of the CNF mat and the full cell are shown in figs. S7 and S8. The full cell is bent to an ~5-mm radius at a 180° bending angle (fig. S9) and returned to the flat state. Using an automatic bending machine, the battery demonstrates 70% capacity retention after 5000 bending cycles and 36% retention after 10,000 cycles (Fig. 4E). In contrast, a similar battery containing slurry-cast electrodes or other types of composite electrodes usually fails after tens or hundreds of bending cycles (Fig. 4F). The direct physical and electrical connection of the electrodeposited LTMO to the current collector (figs. S10 and S11) limits delamination and electrical disconnection during bending, which is why we think that this approach provided such a performance after many flexure cycles.

Electrodeposition of LTMOs in molten salt offers a number of unique advantages relative to aqueous, organic, and other molten salt (halides and carbonates) systems. Because the KOH and LiOH eutectic melt is stable over a relatively large potential window and dissolves well the late first row transition metal oxides starting with Mn and several groups of alkaline earth and lanthanide oxides at a relatively low temperature (~200°C), it is possible to produce a diversity of high-valence oxides in a highly crystalline form by applying an electrical potential. As an example showing the generality of the molten hydroxide electrodeposition approach, a spinel $LiMn_2O_4$ is electrodeposited on a 3D CNF scaffold (fig. S12, A and B) using an electrolyte formed by adding MnO to the LiOH/KOH eutectic melt. Galvanostatic charge/discharge measurements show two well-defined 4-V plateaus (fig. S12C), the signature of high-quality $LiMn_2O_4$, that originate from the Li-ion ordering on one-half of the tetrahedral 8a sites (detailed experiment and modeling information are provided in section SIX). Al-doped $LiCoO_2$ is also synthesized by adding $Al(OH)_3$ to the CoO-containing plating bath (see section SX for details). Al doping is known to improve both stability and energy density of $LiCoO_2$ (*40*, *41*).

CONCLUSION

In summary, we present a new and general molten salt electrodeposition method to synthesize high-quality LTMOs at temperatures far below traditional methods. The new fabrication approach enables fabrication of Li-ion batteries with unique form factors and technologically important properties, including high power, high energy, and high flexibility. The inherent advantage of electrodeposition is that it provides conformal growth of active materials in intimate contact with a current collector, providing opportunities to fabricate underdeveloped but urgently desired electrode structures that other techniques are incapable of creating.

MATERIALS AND METHODS

Electroplating LTMOs

The electroplating bath was prepared by mixing KOH and LiOH with a weight ratio of 5:1 in an Ar-filled glove box. It was then heated at 260°C until the mixture became transparent. About 2 weight % CoO (or MnO) was added into the melt. A Co wire and a Ni plate were used as the reference and the counter electrodes, respectively. During the electroplating, a pulsed waveform was applied between the working and the reference electrodes (1.1-V pulse for 2 s and open-circuit potential for 2 min). We experimentally found that pulsed deposition formed higher-quality material on the planar electrodes than did a constant current or voltage deposition, and pulsed deposition also enabled conformal infilling of the 3D structured electrodes. Depending on the working electrodes, the deposition rate of LTMOs varied from ~10 to ~100 nm per pulse. After the electrodeposition, the sample was washed with deionized water and dried.

Characterization

The electroplated LTMOs were observed using a Hitachi 4800 SEM. XRD patterns were recorded with a PANalytical X'Pert materials research diffractometer. The high-resolution TEM and the electron diffraction patterns of the electroplated LTMOs were collected with a JEOL Cryo 2100 microscope. Raman spectroscopy was carried out using a Horiba confocal Raman imaging microscope. Coin cells were assembled with Celgard 2700 separator and Novolyte electrolyte (1 M $LiPF_6$ in a 1:3:1 ratio of ethylene carbonate, dimethylene carbonate, and diethylene carbonate). Flexible cells were assembled within Kapak SealPAK 400 and 500 series heavy-duty pouches (AMPAC Flexibles). The cells were bent using an IPC flexural endurance tester (CK-700FET, Association Connecting Electronics Industries). All electrochemical measurements were performed with a VMP3 multichannel potentiostat (Bio-Logic Corp.).

SUPPLEMENTARY MATERIALS

Supplementary material for this article is available at http://advances.sciencemag.org/cgi/content/full/3/5/e1602427/DC1

section SI. Plating bath and solubility of transition metal oxides.
section SII. Mesoporous carbon foam.
section SIII. Flexible carbon scaffold.
section SIV. Quasi-reference electrode.
section SV. Thermodynamic modeling.
section SVI. Crystallography of $LiCoO_2$.
section SVII. Scanning electron nanobeam diffraction.
section SVIII. Flexible battery.
section SIX. Electrodeposition of spinel $LiMn_2O_4$.
section SX. Electroplating of Al-doped lithium cobalt oxide.
section SXI. Calculation of energy density of flexible batteries.
fig. S1. Schematic illustration of a flexible CNF.
fig. S2. High-resolution TEM images of the CNF.
fig. S3. High-resolution TEM image and electron diffraction pattern of an electroplated $LiCoO_2$ crystal flake.
fig. S4. Crystallographic structures of O3-, O2-, and spinel-phase lithium cobalt oxides and two superstructures with lithium staging and 2 × 2 periods.
fig. S5. Illustration of the SEND technique.
fig. S6. Cross-sectional SEM image of ~200-μm-thick $LiCoO_2$ electroplated on an Al foil.
fig. S7. Charge/discharge voltage profiles of the CNF anode.
fig. S8. Charge/discharge curves of a $LiCoO_2$/CNF flexible battery.
fig. S9. Optical images of bending tests.
fig. S10. Schematic illustrations of the structure difference between traditional and electroplated flexible batteries.
fig. S11. SEM images of a $LiCoO_2$/CNF cathode before and after 1000 bending cycles.
fig. S12. Materials and electrochemical characterization of the electroplated $LiMn_2O_4$/CNF battery.
fig. S13. The Gibbs free energy of the formation from the elements for $LiMnO_2$.
fig. S14. The Gibbs free energy of $LiMnO_2$.
fig. S15. The potential-pH_2O diagram of the LiOH-KOH-MnO-H_2O melt system.
fig. S16. Materials and electrochemical characterization of the electroplated Al-doped $LiCoO_2$.
table S1. Thermodynamic data used for the LiOH-KOH-CoO system at 260°C.
table S2. Thermodynamic data of the LiOH-KOH-MnO system at 25°C.

table S3. Thermodynamic data of the LiOH-KOH-MnO system at 300°C.
References (*42*–*82*)

REFERENCES AND NOTES

1. Y. Hu, X. Sun, Flexible rechargeable lithium ion batteries: Advances and challenges in materials and process technologies. *J. Mater. Chem. A* **2**, 10712–10738 (2014).
2. T. S. Arthur, D. J. Bates, N. Cirigliano, D. C. Johnson, P. Malati, J. M. Mosby, E. Perre, M. T. Rawls, A. L. Prieto, B. Dunn, Three-dimensional electrodes and battery architectures. *MRS Bull.* **36**, 523–531 (2011).
3. H. Ning, J. H. Pikul, R. Zhang, X. Li, S. Xu, J. Wang, J. A. Rogers, W. P. King, P. V. Braun, Holographic patterning of high-performance on-chip 3D lithium-ion microbatteries. *Proc. Natl. Acad. Sci. U.S.A.* **112**, 6573–6578 (2015).
4. H. Zhang, X. Yu, P. V. Braun, Three-dimensional bicontinuous ultrafast-charge and -discharge bulk battery electrodes. *Nat. Nanotechnol.* **6**, 277–281 (2011).
5. H. Nishide, K. Oyaizu, Toward flexible batteries. *Science* **319**, 737–738 (2008).
6. M.-H. Park, M. Noh, S. Lee, M. Ko, S. Chae, S. Sim, S. Choi, H. Kim, H. Nam, S. Park, J. Cho, Flexible high-energy Li-ion batteries with fast-charging capability. *Nano Lett.* **14**, 4083–4089 (2014).
7. X. Wang, X. Lu, B. Liu, D. Chen, Y. Tong, G. Shen, Flexible energy-storage devices: Design consideration and recent progress. *Adv. Mater.* **26**, 4763–4782 (2014).
8. G. Zhou, F. Li, H.-M. Cheng, Progress in flexible lithium batteries and future prospects. *Energy Environ. Sci.* **7**, 1307–1338 (2014).
9. T. Maiyalagan, K. A. Jarvis, S. Therese, P. J. Ferreira, A. Manthiram, Spinel-type lithium cobalt oxide as a bifunctional electrocatalyst for the oxygen evolution and oxygen reduction reactions. *Nat. Commun.* **5**, 3949 (2014).
10. S. T. Kuk, Y. S. Song, S. Suh, J. Y. Kim, K. Kim, The formation of $LiCoO_2$ on a NiO cathode for a molten carbonate fuel cell using electroplating. *J. Mater. Chem.* **11**, 630–635 (2001).
11. J. Liu, X. Sun, Elegant design of electrode and electrode/electrolyte interface in lithium-ion batteries by atomic layer deposition. *Nanotechnology* **26**, 024001 (2015).
12. J. A. Switzer, Atomic layer electrodeposition. *Science* **338**, 1300–1301 (2012).
13. J. A. Switzer, M. G. Shumsky, E. W. Bohannan, Electrodeposited ceramic single crystals. *Science* **284**, 293–296 (1999).
14. J. Duay, E. Gillette, J. Hu, S. B. Lee, Controlled electrochemical deposition and transformation of hetero-nanoarchitectured electrodes for energy storage. *Phys. Chem. Chem. Phys.* **15**, 7976–7993 (2013).
15. Z. Quan, S. Ohguchi, M. Kawase, H. Tanimura, N. Sonoyama, Preparation of nanocrystalline $LiMn_2O_4$ thin film by electrodeposition method and its electrochemical performance for lithium battery. *J. Power Sources* **244**, 375–381 (2013).
16. J. Yao, T. Takasaki, K. Nishimura, T. Mukai, T. Sakai, X-ray diffraction characterization and battery performances of fiber-type Li-Mn-O electrode for Li-ion battery. *Electrochemistry* **82**, 109–112 (2014).
17. H. Porthault, F. Le Cras, R. Baddour-Hadjean, J. P. Pereira-Ramos, S. Franger, One step synthesis of lamellar *R-3m* $LiCoO_2$ thin films by an electrochemical–hydrothermal method. *Electrochim. Acta* **56**, 7580–7585 (2011).
18. D. Gao, Y. Li, X. Lai, J. Bi, D. Lin, Room-temperature synthesis of crystallized $LiCoO_2$ thin films by electrochemical technique. *J. Alloys Compd.* **509**, 697–703 (2011).
19. J.-H. Lee, K.-S. Han, B.-J. Lee, S.-I. Seo, M. Yoshimura, Fabrication of $LiCoO_2$ films for lithium rechargeable microbattery in an aqueous solution by electrochemical reflux method. *Electrochim. Acta* **50**, 467–471 (2004).
20. K.-S. Han, S.-W. Song, H. Fujita, M. Yoshimura, E. J. Cairns, S.-H. Chang, Direct electroplating of lithium cobalt oxide film on platinum substrate in 100°–200°C aqueous solution. *J. Am. Ceram. Soc.* **85**, 2444–2448 (2002).
21. G. H. A. Therese, P. V. Kamath, Electrochemical synthesis of metal oxides and hydroxides. *Chem. Mater.* **12**, 1195–1204 (2000).
22. M. Nakayama, A. Tanaka, S. Konishi, K. Ogura, Effects of heat-treatment on the spectroscopic and electrochemical properties of a mixed manganese/vanadium oxide film prepared by electrodeposition. *J. Mater. Res.* **19**, 1509–1515 (2004).
23. J. A. Koza, Z. He, A. S. Miller, J. A. Switzer, Electrodeposition of crystalline Co_3O_4—A catalyst for the oxygen evolution reaction. *Chem. Mater.* **24**, 3567–3573 (2012).
24. S. L. Marchiano, A. J. Arvia, Potential/pO^{2-} diagrams of iron, cobalt and nickel in molten sodium nitrite. *Electrochim. Acta* **17**, 861–871 (1972).
25. D. Mohanty, H. Gabrisch, Microstructural investigation of $Li_xNi_{1/3}Mn_{1/3}Co_{1/3}O_2$ ($x \leq 1$) and its aged products via magnetic and diffraction study. *J. Power Sources* **220**, 405–412 (2012).
26. H. Gabrisch, R. Yazami, B. Fultz, Hexagonal to cubic spinel transformation in lithiated cobalt oxide: TEM investigation. *J. Electrochem. Soc.* **151**, A891–A897 (2004).
27. H. Gabrisch, R. Yazami, B. Fultz, A transmission electron microscopy study of cycled $LiCoO_2$. *J. Power Sources* **119–121**, 674–679 (2003).
28. Y. Shao-Horn, S. Levasseur, F. Weill, C. Delmas, Probing lithium and vacancy ordering in O_3 layered Li_xCoO_2 ($x \approx 0.5$): An electron diffraction study. *J. Electrochem. Soc.* **150**, A366–A373 (2003).
29. H. Wang, Y.-I. Jang, B. Huang, D. R. Sadoway, Y.-M. Chiang, TEM study of electrochemical cycling-induced damage and disorder in $LiCoO_2$ cathodes for rechargeable lithium batteries. *J. Electrochem. Soc.* **146**, 473–480 (1999).
30. A. Van der Ven, M. K. Aydinol, G. Ceder, First-principles evidence for stage ordering in Li_xCoO_2. *J. Electrochem. Soc.* **145**, 2149–2155 (1998).
31. D. Carlier, I. Saadoune, L. Croguennec, M. Ménétrier, E. Suard, C. Delmas, On the metastable O2-type $LiCoO_2$. *Solid State Ion.* **144**, 263–276 (2001).
32. X. Lu, Y. Sun, Z. Jian, X. He, L. Gu, Y.-S. Hu, H. Li, Z. Wang, W. Chen, X. Duan, L. Chen, J. Maier, S. Tsukimoto, Y. Ikuhara, New insight into the atomic structure of electrochemically delithiated O3-$Li_{(1-x)}CoO_2$ ($0 \leq x \leq 0.5$) nanoparticles. *Nano Lett.* **12**, 6192–6197 (2012).
33. J. M. Paulsen, J. R. Mueller-Neuhaus, J. R. Dahn, Layered $LiCoO_2$ with a different oxygen stacking (O_2 structure) as a cathode material for rechargeable lithium batteries. *J. Electrochem. Soc.* **147**, 508–516 (2000).
34. R. Baddour-Hadjean, J.-P. Pereira-Ramos, Raman microspectrometry applied to the study of electrode materials for lithium batteries. *Chem. Rev.* **110**, 1278–1319 (2010).
35. R. J. Gummow, M. M. Thackeray, W. I. F. David, S. Hull, Structure and electrochemistry of lithium cobalt oxide synthesized at 400°C. *Mater. Res. Bull.* **27**, 327–337 (1992).
36. R. J. Gummow, D. C. Liles, M. M. Thackeray, Spinel versus layered structures for lithium cobalt oxide synthesized at 400°C. *Mater. Res. Bull.* **28**, 235–246 (1993).
37. A. Nyman, T. G. Zavalis, R. Elger, M. Behm, G. Lindbergh, Analysis of the polarization in a Li-ion battery cell by numerical simulations. *J. Electrochem. Soc.* **157**, A1236–A1246 (2010).
38. M. Singh, J. Kaiser, H. Hahn, Thick electrodes for high energy lithium ion batteries. *J. Electrochem. Soc.* **162**, A1196–A1201 (2015).
39. K. G. Gallagher, S. E. Trask, C. Bauer, T. Woehrle, S. F. Lux, M. Tschech, P. Lamp, B. J. Polzin, S. Ha, B. Long, Q. Wu, W. Lu, D. W. Dees, A. N. Jansen, Optimizing areal capacities through understanding the limitations of lithium-ion electrodes. *J. Electrochem. Soc.* **163**, A138–A149 (2016).
40. G. Ceder, Y.-M. Chiang, D. R. Sadoway, M. K. Aydinol, Y.-I. Jang, B. Huang, Identification of cathode materials for lithium batteries guided by first-principles calculations. *Nature* **392**, 694–696 (1998).
41. W.-S. Yoon, K.-K. Lee, K.-B. Kim, Structural and electrochemical properties of $LiAl_yCo_{1-y}O_2$ cathode for Li rechargeable batteries. *J. Electrochem. Soc.* **147**, 2023–2028 (2000).
42. J. Chivot, L. Mendoza, C. Mansour, T. Pauporte, M. Cassir, New insight in the behaviour of Co–H_2O system at 25–150°C, based on revised Pourbaix diagrams. *Corros. Sci.* **50**, 62–69 (2008).
43. M. H. Miles, Exploration of molten hydroxide electrochemistry for thermal battery applications. *J. Appl. Electrochem.* **33**, 1011–1016 (2003).
44. H. Hayashi, S. Yoshizawa, Studies on oxygen reduction in molten NaOH. *Electrochim. Acta* **28**, 149–153 (1983).
45. P. G. Zambonin, Reversible oxygen electrode systems in molten salts. *J. Electroanal. Chem. Interfacial Electrochem.* **33**, 243–251 (1971).
46. H. Hayashi, S. Yoshizawa, Y. Ito, Electrochemical studies on molten sodium-hydroxide. *J. Electroanal. Chem.* **124**, 229–235 (1981).
47. B. L. Tremillon, Acid-base effects in molten electrolytes, in *Molten Salt Chemistry: An Introduction and Selected Applications,* G. Mamantov, R. Marassi, Eds. (D. Reidel Publishing Company, 1987), pp. 279–303.
48. I. I. Barin, *Thermochemical Data of Pure Substances* (VCH Verlagsgesellschaft mbH, ed. 3, 1997).
49. Y. C. Zhang, H. Tagawa, S. Asakura, J. Mizusaki, H. Narita, Solid-state CO_2 sensor with Li_2CO_3-Li_3PO_4-$LiAlO_2$ electrolyte and $LiCoO_2$-Co_3O_4 as solid reference electrode. *J. Electrochem. Soc.* **144**, 4345–4350 (1997).
50. M. Wang, A. Navrotsky, Enthalpy of formation of $LiNiO_2$, $LiCoO_2$ and their solid solution, $LiNi_{1-x}Co_xO_2$. *Solid State Ion.* **166**, 167–173 (2004).
51. S. R. Alvarado, Y. Guo, T. P. A. Ruberu, A. Bakac, J. Vela, Photochemical versus thermal synthesis of cobalt oxyhydroxide nanocrystals. *J. Phys. Chem. C* **116**, 10382–10389 (2012).
52. Z. P. Xu, H. C. Zeng, Thermal evolution of cobalt hydroxides: A comparative study of their various structural phases. *J. Mater. Chem.* **8**, 2499–2506 (1998).
53. J. Balej, J. Divisek, Diagrams *E*-r-m_{KOH} for cobalt at 25–125°C and at total pressure of 1–30 bar. *Collect. Czech. Chem. Commun.* **62**, 1663–1676 (1997).
54. H. Chen, thesis, Stony Brook University (2009).
55. H. Gabrisch, Y. Ozawa, R. Yazami, Crystal structure studies of thermally aged $LiCoO_2$ and $LiMn_2O_4$ cathodes. *Electrochim. Acta* **52**, 1499–1506 (2006).
56. A. Mendiboure, C. Delmas, P. Hagenmuller, New layered structure obtained by electrochemical deintercalation of the metastable $LiCoO_2$ (O2) variety. *Mater. Res. Bull.* **19**, 1383–1392 (1984).
57. J.-M. Zuo, J. Tao, Scanning electron nanodiffraction and diffraction imaging, in *Scanning Transmission Electron Microscopy Imaging and Analysis,* S. J. Pennycook, P. D. Nellist, Eds. (Springer, 2011), chap. 9.
58. L. Wang, T. Maxisch, G. Ceder, A first-principles approach to studying the thermal stability of oxide cathode materials. *Chem. Mater.* **19**, 543–552 (2007).

59. Y. Kim, D. Kim, S. Kang, Experimental and first-principles thermodynamic study of the formation and effects of vacancies in layered lithium nickel cobalt oxides. *Chem. Mater.* **23**, 5388–5397 (2011).
60. R. Xiao, H. Li, L. Chen, Density functional investigation on Li_2MnO_3. *Chem. Mater.* **24**, 4242–4251 (2012).
61. R. C. Longo, F. T. Kong, K. C. Santosh, M. S. Park, J. Yoon, D.-H. Yeon, J.-H. Park, S.-G. Doo, K. Cho, Phase stability of Li–Mn–O oxides as cathode materials for Li-ion batteries: Insights from ab initio calculations. *Phys. Chem. Chem. Phys.* **16**, 11218–11227 (2014).
62. M. J. Wang, A. Navrotsky, LiMO_2 (M = Mn, Fe, and Co): Energetics, polymorphism and phase transformation. *J. Solid State Chem.* **178**, 1230–1240 (2005).
63. J. Fischer, K. Chang, J. Ye, S. Ulrich, C. Ziebert, D. Music, B. Hallstedt, H. J. Seifert, Structural transformation of sputtered *o*-$LiMnO_2$ thin-film cathodes induced by electrochemical cycling. *Thin Solid Films* **549**, 263–267 (2013).
64. S. Crouch-baker, R. A. Huggins, Thermodynamic rationalization of molten-salt electrodeposition in oxide-based systems. *J. Mater. Res.* **4**, 1495–1504 (1989).
65. K. E. Spear, T. M. Besmann, E. C. Beahm, Thermochemical modeling of glass: Application to high-level nuclear waste glass. *MRS Bull.* **24**, 37–44 (1999).
66. H. Yokokawa, N. Sakai, K. Yamaji, T. Horita, M. Ishikawa, Thermodynamic determining factors of the positive electrode potential of lithium batteries. *Solid State Ion.* **113–115**, 1–9 (1998).
67. N. A. Godshall, I. D. Raistrick, R. A. Huggins, Relationships among electrochemical, thermodynamic, and oxygen potential quantities in lithium-transition metal-oxygen molten salt cells. *J. Electrochem. Soc.* **131**, 543–549 (1984).
68. G. Róg, W. Kucza, A. Kozlowska-Róg, The standard Gibbs free energy of formation of lithium manganese oxides at the temperatures of (680, 740 and 800) K. *J. Chem. Thermodyn.* **36**, 473–476 (2004).
69. J. A. Koza, I. P. Schroen, M. M. Willmering, J. A. Switzer, Electrochemical synthesis and nonvolatile resistance switching of Mn_3O_4 thin films. *Chem. Mater.* **26**, 4425–4432 (2014).
70. Y.-I. Jang, B. Huang, H. Wang, G. R. Maskaly, G. Ceder, D. R. Sadoway, Y.-M. Chiang, H. Liu, H. Tamura, Synthesis and characterization of $LiAl_yCo_{1-y}O_2$ and $LiAl_yNi_{1-y}O_2$. *J. Power Sources* **81–82**, 589–593 (1999).
71. S.-T. Myung, N. Kumagai, S. Komaba, H.-T. Chung, Effects of Al doping on the microstructure of $LiCoO_2$ cathode materials. *Solid State Ion.* **139**, 47–56 (2001).
72. C.-H. Han, Y.-S. Hong, K. Kim, Cyclic performances of HT-$LiCo_{0.8}M_{0.2}O_2$ (M=Al, Ni) powders prepared by the molten salt synthesis method. *Solid State Ion.* **159**, 241–247 (2003).
73. Y. I. Jang, B. Huang, H. Wang, D. R. Sadoway, G. Ceder, Y.-M. Chiang, H. Liu, H. Tamura, $LiAl_yCo_{1-y}O_2$ ($R\bar{3}m$) intercalation cathode for rechargeable lithium batteries. *J. Electrochem. Soc.* **146**, 862–868 (1999).
74. A. E. Ostfeld, A. M. Gaikwad, Y. Khan, A. C. Arias, High-performance flexible energy storage and harvesting system for wearable electronics. *Sci. Rep.* **6**, 26122 (2016).
75. M. Li, F. Pan, E. S. G. Choo, Y. Lv, Y. Chen, J. Xue, Designed construction of a graphene and iron oxide freestanding electrode with enhanced flexible energy-storage performance. *ACS Appl. Mater. Interfaces* **8**, 6972–6981 (2016).
76. H. Wu, Q. Meng, Q. Yang, M. Zhang, K. Lu, Z. Wei, Large-area polyimide/SWCNT nanocable cathode for flexible lithium-ion batteries. *Adv. Mater.* **27**, 6504–6510 (2015).
77. X. Tang, F. Yan, Y. Wei, M. Zhang, T. Wang, T. Zhang, Encapsulating Sn_xSb nanoparticles in multichannel graphene-carbon fibers as flexible anodes to store lithium ions with high capacities. *ACS Appl. Mater. Interfaces* **7**, 21890–21897 (2015).
78. A. M. Gaikwad, B. V. Khau, G. Davies, B. Hertzberg, D. A. Steingart, A. C. Arias, A high areal capacity flexible lithium-ion battery with a strain-compliant design. *Adv. Energy Mater.* **5**, 1401389 (2015).
79. J. Ren, Y. Zhang, W. Bai, X. Chen, Z. Zhang, X. Fang, W. Weng, Y. Wang, H. Peng, Elastic and wearable wire-shaped lithium-ion battery with high electrochemical performance. *Angew. Chem. Int. Ed.* **53**, 7864–7869 (2014).
80. H. Lin, W. Weng, J. Ren, L. Qiu, Z. Zhang, P. Chen, X. Chen, J. Deng, Y. Wang, H. Peng, Twisted aligned carbon nanotube/silicon composite fiber anode for flexible wire-shaped lithium-ion battery. *Adv. Mater.* **26**, 1217–1222 (2014).
81. Y. H. Ding, H. M. Ren, Y. Y. Huang, F. H. Chang, P. Zhang, Three-dimensional graphene/$LiFePO_4$ nanostructures as cathode materials for flexible lithium-ion batteries. *Mater. Res. Bull.* **48**, 3713–3716 (2013).
82. N. Li, Z. Chen, W. Ren, F. Li, H.-M. Cheng, Flexible graphene-based lithium ion batteries with ultrafast charge and discharge rates. *Proc. Natl. Acad. Sci. U.S.A.* **109**, 17360–17365 (2012).

Acknowledgments: H.Z. thanks H. Chen (Georgia Tech) for the insightful discussions. **Funding:** Work at the University of Illinois Urbana Champaign is supported by the Basic Energy Sciences, Office of Science, U.S. Department of Energy, under award DE-FG02-07ER46741. Work at Nanjing University is supported by the Thousand Youth Talents Plan (no. 128010), the National Materials Genome Project (2016YFB0700600), the Jiangsu Outstanding Youth Funds (BK20160012), and the "Jiangsu Shuangchuang" Program. S.W. and P.W. acknowledge the support from the National Natural Science Foundation of China (11474147), the National Basic Research Program of China (2015CB654901). We thank the High Performance Computing Center of Nanjing University for numerical calculations. **Author contributions:** H.Z. conceived the first successful bath chemistry. H.Z., H.N., and P.V.B. built off this discovery and supervised the work. H.Z., H.N., and J.B. supervised the materials synthesis. Z.S., C.K., Y.H., J.E., J.D., T.S., and P.S. synthesized the materials. Y.H., J.E., J.D., T.S., and S.X. performed electrochemical and mechanical characterizations. Y.-T.S., J.-M.Z., X.H., Y.C., S.W., and J.L. performed materials characterizations and assisted in the interpretation of results. H.Z., H.N., and P.V.B. wrote the manuscript. All authors have discussed the results and commented on the manuscript. **Competing interests:** P.V.B has an equity stake in and is a co-founder, the chief technology officer, and a member of the Board of Directors of Xerion Advanced Battery Corp. H.N. is the Director of Research and Development at Xerion Advanced Battery Corp. J.B. is a shareholder and the chief executive officer of Xerion Advanced Battery Corp. J.E. is an employee of Xerion Advanced Battery Corp. Xerion Advanced Battery Corporation has an application for a patent related to this work, US 2016/0028081 A1 (application no. 14/806,066, filed on 22 July 2015). **Data and materials availability:** All data needed to evaluate the conclusions in the paper are present in the paper and/or the Supplementary Materials. Additional data related to this paper may be requested from the authors. Samples and characterization data are archived and can be made available upon request.

Submitted 3 October 2016
Accepted 22 March 2017
Published 12 May 2017
10.1126/sciadv.1602427

Citation: H. Zhang, H. Ning, J. Busbee, Z. Shen, C. Kiggins, Y. Hua, J. Eaves, J. Davis III, T. Shi, Y.-T. Shao, J.-M. Zuo, X. Hong, Y. Chan, S. Wang, P. Wang, P. Sun, S. Xu, J. Liu, P. V. Braun, Electroplating lithium transition metal oxides. *Sci. Adv.* **3**, e1602427 (2017).

Electroplating lithium transition metal oxides

Huigang Zhang, Hailong Ning, John Busbee, Zihan Shen, Chadd Kiggins, Yuyan Hua, Janna Eaves, Jerome Davis III, Tan Shi, Yu-Tsun Shao, Jian-Min Zuo, Xuhao Hong, Yanbin Chan, Shuangbao Wang, Peng Wang, Pengcheng Sun, Sheng Xu, Jinyun Liu and Paul V. Braun (May 12, 2017)

Sci Adv 2017, 3:.
doi: 10.1126/sciadv.1602427